AIAA JOURNAL
Vol. 56, No. 7, July 2018

Measurement of Flow Perturbation Spectra in Mach 4.5 Corner Separation Zone

Brock Hedlund,* Alec Houpt,* Stanislav Gordeyev,† and Sergey Leonov‡
University of Notre Dame, Notre Dame, Indiana 46556

DOI: 10.2514/1.J056576

Characterization of the $M = 4.5$ flow over a flat-plate model with a 30 deg compression ramp was performed with low-enthalpy ($T_0 = 300$ K) and high-enthalpy ($T_0 = 800$–1250 K) flow conditions for a wide range of unit Reynolds numbers ($Re_l = 4 \cdot 10^5 - 1 \cdot 10^7$ m^{-1}). Three measurement techniques were employed to measure the frequency spectrum of flow perturbations: a high-frequency Shack–Hartmann wavefront sensor (aerooptical method), high-frequency PCB™ pressure sensors, and a laser differential interferometer. The magnitude and frequency of flow oscillations measured by all three methods provide comprehensive and complementary results in determining spectra of gas disturbances within the flow. Of these measurement methods, the Shack–Hartmann wavefront sensor is shown to be the most suitable tool for analysis of the high-speed flow. Aerooptical measurements detect modification to the flow structure when plasma actuation is employed or when Re_l is varied. In this work, flow characterization by the Shack–Hartmann sensor at individual points over the ramp has shown three flow regimes depending on the unit Reynolds number: turbulent, transitional, and laminar. At higher Re_l, the freestream disturbances become strong enough to significantly affect the perturbations in the boundary-layer and the separation zone on the compression ramp. Frequency spectrum measurements during high-frequency plasma actuation ($F = 100$ kHz) indicate amplification of the perturbations from the natural state that occur over the separation region.

Nomenclature

a	=	speed of sound, m/s
$C(\tau)$	=	correlation function
E	=	pulse energy, mJ
F	=	repetition frequency, kHz
f	=	frequency, Hz
M	=	Mach number
$\dot{m}$	=	mass flow rate, kg/s
P	=	static pressure, mbar
$P_{xx}(f)$	=	power spectral density
P_0	=	stagnation pressure, bar
Re_l	=	unit Reynolds number, m^{-1}
Re_x	=	Reynolds number based on model length
T	=	temperature, K
T_0	=	stagnation temperature, K
t	=	time, pulse duration, s
U	=	voltage, V
U_∞	=	freestream velocity, m/s
v	=	velocity, m/s
W_{av}	=	average power, W
α, β	=	generic angles, deg
$\Gamma(f)$	=	coherence function
δ	=	boundary-layer thickness, mm
λ	=	laser wavelength, nm
ξ_M	=	similarity parameter
ρ	=	gas density, kg/m^3
$\check{\rho}$	=	wall-normal component of deflection angle (arbitrary units)
τ	=	time delay, s

I. Introduction

METHODS of supersonic and hypersonic boundary-layer (BL) flow control by electrical discharges have previously been studied extensively [1–4], showing a plausible controlling effect due to a nonuniform localized heating of the near-surface gas layer. Of a particular interest to this study is the effect of a pulsed plasma actuator on the flow oscillations along a flat plate leading up to a compression ramp with a separation zone in hypersonic flow. Preliminary studies have characterized the oscillatory flow structure in the flat-plate boundary-layer and the corner separation zone [5,6]. The boundary-layer over flat-plate compression ramp geometries is of interest for its role in scramjet inlets for an effective flow conditioning before combustion. Several publications have shown that the generation of streamwise vorticity within the flow leads to an accelerated transition of the boundary-layer to a turbulent state [7–9], which is desirable for both a reduction of the boundary-layer separation and fuel mixing farther downstream. The result of reduced flow separation for turbulent supersonic boundary-layer interaction with a compression ramp has been analyzed previously in [10]. It was also shown in [5] that the shallow cavity discharge (SCD) is a suitable method for the generation of high-frequency fluctuations of gas density in the flow, when operated at repetition frequencies greater than those of naturally occurring perturbations in the flowfield.

The flowfield characteristics over supersonic and hypersonic compression ramps have been discussed in many studies [11–15] involving the evolution of boundary-layer perturbations over a flat plate. The presence of the first mode of instabilities (Tollmien–Schlichting waves) and, in this case especially, second-mode instabilities (of acoustic nature) are known to be dominant and grow in the hypersonic boundary-layer along a flat plate leading up to the corner separation zone [16]. Within the separation zone, dynamics of the instabilities are quite complex, but their growth is known to be neutral, with amplification of only discrete acoustic modes [12]. If laser beams are directed spanwise across the flow, the amplitude spectra of the overall aerooptical distortions exhibit a growth in fluctuations near the separation and reattachment regions [17]. An important feature of the current work is that it examines flow conditions with a high level of initial perturbations in the core flow, which are typical for most wind tunnel tests and can simulate a flow

Presented as Paper 2017-3341 at the 48th AIAA Plasmadynamics and Lasers Conference, Denver, CO, 5–9 June 2017; received 28 July 2017; revision received 2 February 2018; accepted for publication 12 February 2018; published online 12 April 2018. Copyright © 2018 by the authors. Published by the American Institute of Aeronautics and Astronautics, Inc., with permission. All requests for copying and permission to reprint should be submitted to CCC at www.copyright.com; employ the ISSN 0001-1452 (print) or 1533-385X (online) to initiate your request. See also AIAA Rights and Permissions www.aiaa.org/randp.

*Graduate Student, Department of Aerospace and Mechanical Engineering, Institute for Flow Physics and Control. Student Member AIAA.

†Associate Professor, Department of Aerospace and Mechanical Engineering, Institute for Flow Physics and Control. Associate Fellow AIAA.

‡Research Professor, Department of Aerospace and Mechanical Engineering, Institute for Flow Physics and Control. Associate Fellow AIAA.

Downloaded by UNIVERSITY OF NOTRE DAME on July 2, 2018 | http://arc.aiaa.org | DOI: 10.2514/1.J056576

Downloaded by UNIVERSITY OF NOTRE DAME on July 2, 2018 | http://arc.aiaa.org | DOI: 10.2514/1.J056576

environment such as an operation in the wake of another vehicle or air with high levels of dust. Characterization of such flows is challenging, the numerical simulation is difficult, and the resulting flow structure is not immediately obvious [18,19].

In this study, measurements of the flow perturbations, with primary interest on the oscillations occurring in the separation zone, are performed by three diagnostic tools:

1) A Shack–Hartmann (SH) wavefront (WF) sensor is used to determine overall aerooptical distortions in the spanwise direction; these time-resolved distortions are essentially the density fields, averaged in the spanwise direction. The ability of this method to measure the density oscillations in spanwise-uniform turbulent flows was demonstrated in [20]. This optical wavefront sensing is revealed to be a proper candidate for nonintrusive high-frequency measurements in hypersonic conditions due to the expectation of spanwise uniformity over the flat plate and the sensor's sensitivity to gas density gradients. In addition, the wavefront sensor is capable of providing high spatial resolution and up to 1 MHz frequency response, limited only by the imaging camera's technical capability.

2) The measurement of high-frequency pressure perturbations is by means of surface-mounted pressure sensors, a method that is routinely used in many experimental studies [21–23]. Using 1 MHz response PCB™ sensors, pressure perturbations along the model surface can be detected and analyzed in the frequency domain.

3) Laser differential interferometry (LDI), which is another optical sensing technique, has been proven to be an effective tool in measuring high-frequency density fluctuations in supersonic and hypersonic flows [24–27]. The LDI measures the phase difference between two orthogonally polarized laser beams. Given that everything in the setup of the LDI remains constant except for the passing density perturbations of the flow in the probe volume, fluctuations in the optical path difference lead to changes in the phase difference between the beams and can be directly related to fluctuations of the flow density. LDI systems can measure frequencies of flow perturbations over 1 MHz and optical path differences on the order of 10 nm. This makes it another suitable tool for spectral analysis of low-density, high-speed flows.

II. Experimental Methods

A. Test Arrangement

Tests were conducted in the hypersonic wind tunnel ACT-1 at the University of Notre Dame [28]. Different interchangeable nozzles allow for testing at Mach 4.5, 6, and 9. This study was focused on $M = 4.5$ conditions. The ACT-1 facility uses a dc arc heater to generate high-enthalpy flow, simulating conditions similar to a low-density hypersonic flight. In these tests, the stagnation temperatures ranged from $T_0 = 800$–1250 K (high enthalpy) to $T_0 = 300$ K (low enthalpy). Other relevant test conditions include unit Reynolds number $Re_l = 3 \cdot 10^6$–$1 \cdot 10^7$ m^{-1} (low enthalpy) or $Re_l = 4 \cdot 10^5$–$2 \cdot 10^6$ m^{-1} (high enthalpy) and stagnation pressure 0.8 bar < P_0 < 5.5 bar. Nitrogen was used as a working gas in these tests. The flow characteristics for varying stagnation pressures are shown in Table 1, with the flow velocities determined by direct measurements using SH wavefront sensor at the nozzle exit [6]. Specifically, this approach used a multipoint cross-correlation technique [29] to allow for the measurement of convective speeds of naturally occurring, optically active small-scale turbulent structures in the freestream exiting the nozzle and invoking Taylor's frozen field assumption. While the Reynolds number Re_x is calculated based on the model length from the leading edge to the ramp corner, the unit Reynolds number Re_l is used to describe the flow conditions independently of model length scales.

Figure 1 presents the layout of the test setup. The experimental configuration for testing includes a compression ramp model mounted in the test section of ACT-1 (see Fig. 2). The model consists of a flat plate with a sharp leading edge and a lower surface at a fixed angle $\alpha = 15$ deg. The second wedge is interchangeable and is mounted on top of the flat plate to form the compression ramp of angle $\beta = 30$ deg. In total, the model measures as follows: length $L = 229$ mm, width $W = 102$ mm, and height $H = 19$ mm. The pressure sensors are flush mounted at the locations labeled CH1, CH2, and CH3 in Figs. 1 and 2 to provide measurements on the flat-plate surface both in the boundary-layer and within the corner separation zone. Along the flow axis, the sensors are mounted 20, 10, and 2.5 mm upstream of the ramp corner, respectively.

A high-resolution schlieren system was used to observe the basic flow structure. The system consists of a pulsed near-infrared (NIR) laser diode module (LS8-10-150-S10-00; 850 nm, 10 W peak power, 150 ns pulse duration) and a framing camera (Basler acA2040-180 km-NIR, up to 187 frames/s at full 2048×2048 px resolution). A typical image has an exposure time of 24 μs with the laser pulse duration less than 0.1 μs, thus freezing the flow in time. Schlieren images indicate the presence of not only a separation zone in the corner but also a region of large density gradients downstream, related to the compression shock wave. It is challenging to use schlieren visualization in such a low-density environment. To increase the signal-to-noise ratio and improve the overall quality of the final image, tens of images were averaged together. In Fig. 3, the average schlieren visualization image shows the overall flow pattern around the model, with the associated shocks and the separation region near the corner of compression surfaces.

B. Electrical Discharge

The SCD actuator [30] was used to generate artificial high-frequency disturbances in the flow. This discharge method allows for adjustment of the frequency of pulsed plasma operation for optimization in different flow conditions. The duration of pulses was as short as $t = 4$ μs to produce pointwise disturbances. The pin anodes were arranged in three small cavities on the metallic surface of

Table 1 Flow characteristics for cold and heated flow in ACT-1

Low enthalpy									
				At nozzle exit					
P_0, bar	$\dot{m}$, kg/s	T_0, K	Re_x	T, K	v, m/s	a, m/s	P, mbar	ρ, kg/m^3	Re_l, m^{-1}
0.9	0.028	293	2.10E + 05	58	699	155	3.11	0.018	2.70E + 06
1.5	0.037	293	2.80E + 05	58	699	155	5.18	0.03	3.50E + 06
1.9	0.048	293	3.60E + 05	58	699	155	6.56	0.038	4.60E + 06
2.5	0.06	293	4.50E + 05	58	699	155	8.64	0.05	5.80E + 06
3.2	0.078	293	5.80E + 05	58	699	155	11.06	0.064	7.50E + 06
4	0.096	293	7.20E + 05	58	699	155	13.82	0.08	9.20E + 06
5.5	0.134	293	1.00E + 06	58	699	155	19	0.11	1.30E + 07
High enthalpy									
				At nozzle exit					
P_0, bar	$\dot{m}$, kg/s	T_0, K	Re_x	T, K	v, m/s	a, m/s	P, mbar	ρ, kg/m^3	Re_l, m^{-1}
1.5	0.02	1238	3.60E + 04	245	1437	319	5.18	0.007	4.60E + 05
2.25	0.032	906	7.60E + 04	179	1229	273	7.77	0.015	9.60E + 05
3	0.043	880	1.00E + 05	174	1211	269	10.37	0.02	1.30E + 06
3.25	0.049	835	1.20E + 05	165	1180	262	11.23	0.023	1.60E + 06

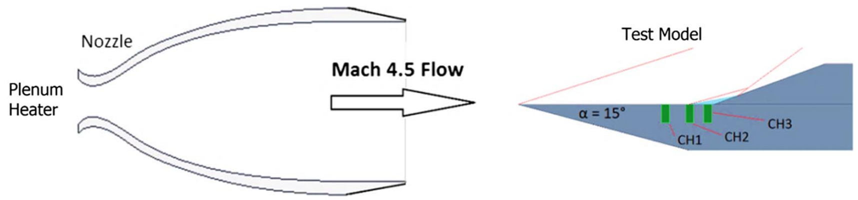

Fig. 1 Side view of experimental arrangement.

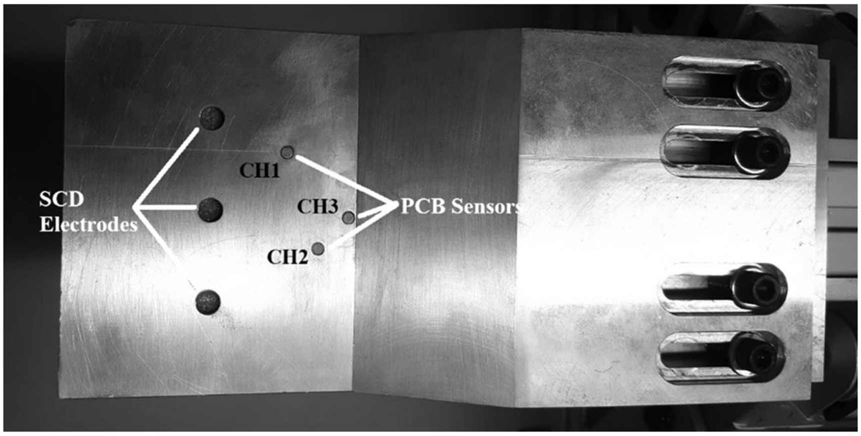

Fig. 2 Model in the test section of ACT-1 at the University of Notre Dame.

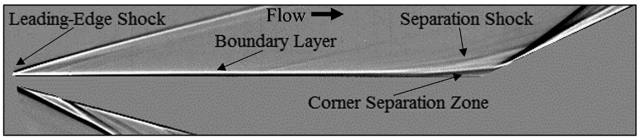

Fig. 3 Averaged schlieren image representing major flow features.

the model spaced 22 mm apart in the spanwise direction, 6 mm in diameter and 3 mm in depth, and 40.5 mm upstream of the ramp corner. During operation, a filamentary plasma extended from the insulated pins to the metallic surface of the model and interacted with the near-surface gas layer. It had a pointwise discharge geometry, reasonably low applied voltage, and a sufficient magnitude of the disturbances produced. A time-resolved image of the SCD in $M = 4.5$ flow taken by an Andor iStar intensified charge-coupled device camera at an exposure of 1 μs is shown in Fig. 4a. At $F = 50$–100 kHz, the discharge worked as a push–pull plasma minijet. At lower frequencies of repetition, another operation mode was observed [30,31], currently considered as a cathode sheath pattern in which a thin layer of plasma covered most of the model surface.

Typical records of the electric parameters in $M = 4.5$ flow are shown in Fig. 5a for a frequency of repetition $F = 100$ kHz. The pulse energy and average power were calculated based on these data, as is shown in Fig. 5b. The discharge parameters were as follows: frequency of repetition $F = 10$–100 kHz, pulse duration $t = 4$ μs,

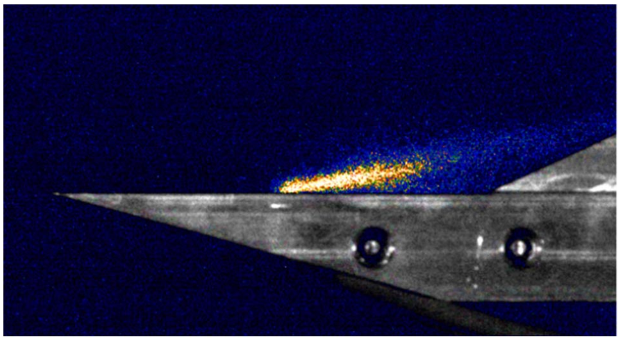

Fig. 4 SCD in $M = 4.5$ flow in plasma minijet operation mode: exposure 1 μs and delay time 3 μs (within the electric pulse).

voltage $U < 1$ kV, pulse energy $E = 0.8$–1.2 mJ/unit, and average power $W_{\mathrm{av}} < 400$ W.

C. Flow Measurements

Series of tests were carried out to collect the data on flow perturbations by means of three nonintrusive measuring systems. These included optical measurements made by a SH wavefront sensor and LDI and flush-mounted surface pressure sensors. Measurements of the flow perturbations were conducted near and within the separation zone to characterize high-frequency responses and to observe changes in the boundary-layer separation zone near the ramp corner. Data collected within the separation zone were then compared with the freestream measurements and baseline data to indicate differences in the spectra (see Figs. 7, 8, and 10). In addition, the comparison between measurements made by the surface-mounted pressure sensors and LDI allows for a more comprehensive analysis of pressure and density dynamics within the flow than previously studied [5]. The data measured by these three methods are presented in the form of spectra $\hat{x}(f)$ of signal $x(t)$ calculated by method of a fast Fourier transform to study the amplitude and the range of frequencies of dominantly occurring perturbations in the flowfield. This is computed by the function

$$\hat{x}(f) = \int_{-\infty}^{\infty} e^{-i2\pi f t} \cdot x(t) \cdot \mathrm{d}t \tag{1}$$

where $x(t)$ represents a measured signal in the time domain. Using the transformed data, the amplitude of perturbations is then computed on a one-sided spectrum with a rectangular window function. Additionally, the power spectral density (PSD) is computed to further highlight variations in spectral energy as a function of frequency. This representation is commonly used in publications on BL transition [17,21,22,32]. It is computed as

$$\mathrm{PSD} = P_{xx}(f) = |\hat{x}(f)|^2 \cdot f \tag{2}$$

Aerooptical measurements were performed using a high-speed SH wavefront sensor [20,33]; the layout is shown in Fig. 6. The system consisted of a laser beam, expanded to a 50-mm-diam collimated beam and passed along the spanwise direction over the corner region of the model mounted in the test section. The spanwise beam

Downloaded by UNIVERSITY OF NOTRE DAME on July 2, 2018 | http://arc.aiaa.org | DOI: 10.2514/1.J056576

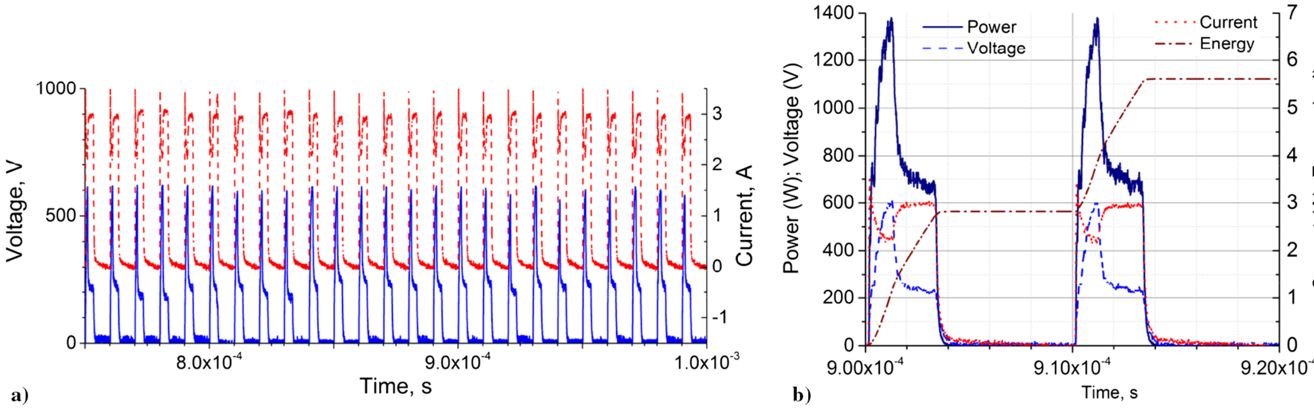

Fig. 5 a) Voltage–current time series of the SCD operation at $F = 100$ kHz; b) discharge pulse power and energy for three SCDs.

Downloaded by UNIVERSITY OF NOTRE DAME on July 2, 2018 | http://arc.aiaa.org | DOI: 10.2514/1.J056576

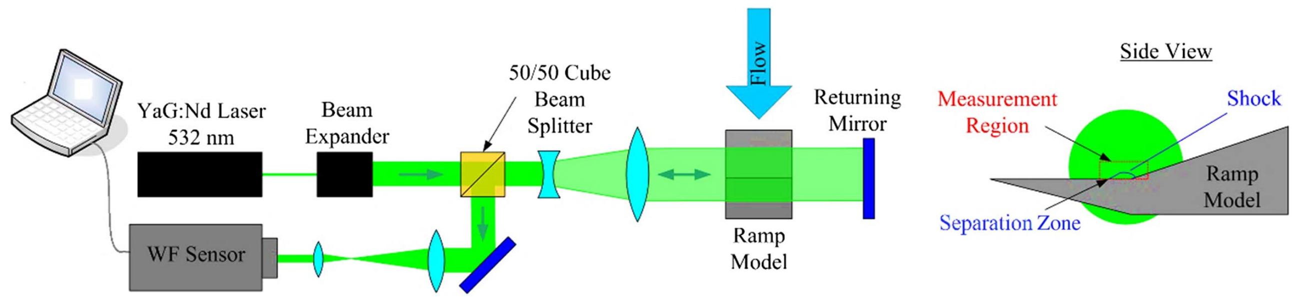

Fig. 6 Schematic of spanwise aerooptical measurements using SH wavefront sensor.

propagation was employed for two reasons. First, the mean flow was expected to be primarily spanwise uniform. Second, as the beam traversed the 4-in.-long region of the flow, overall aerooptical distortions became stronger, thus improving the signal-to-noise ratio [20]. After exiting the test section, the beam was reflected off the return mirror, which sent the beam back along the same path. This so-called double-path setup amplified the aerooptical signal by a factor of 2 and also simplified the optical setup. The returning beam was split off using a cube beam splitter, sent though a contracting telescope, which reduced the beam size to 12.5 mm in diameter, corresponding to a magnification ratio of 4 and recorded by a Phantom v1611 high-speed digital camera. The camera had a 38 mm focal length, 70×60 lenslet array with a 0.3 mm pitch, 100% fill ratio, attached to it. After passing through the lenslet array, the beam was split into subaperture beams and focused on the camera sensor, creating a series of dots. The location of the dot was proportional to the local gradient of the overall wavefront, imposed on the laser beam. Thus, a motion of the dot corresponded to temporal evolution of local wavefront gradients or deflection angles caused by aerooptical distortions, averaged over the lenslet area; the averaging area corresponded to 1.2×1.2 mm over the model. To achieve the high sampling rate of 531 kHz, only a small portion of the image (128×64 pixels) was acquired for the full duration of the wind tunnel run. Centroids of dots' locations were extracted and converted into the local deflection angles using in-house software; more details are presented in [20,34,35].

Unlike the LDI technique, which is discussed in the following, the SH wavefront sensor measures two quantities, the streamwise and the spanwise deflection angles, per each point, and thus provides more information about the flow. Also, any corrupting effects from mechanically related vibrations imposed on the laser beam are easily removed from SH wavefront data [29]; these corrupting effects are still present in the data for LDI. Therefore, it is the most adequate wavefront sensor to measure aerooptical distortions [35].

Flow perturbations acquired by the SH sensor were analyzed at different points within the flowfield (shown in Fig. 12) to identify the spectra of flow perturbations and dominant frequencies of oscillations occurring in the flow (see Fig. 7). The nondimensional frequency, defined by $f \cdot \delta / U_\infty$, allowed for a simple frequency analysis and comparison [32,36]. The estimated boundary-layer thickness δ was chosen as a scaling factor to match the expected length scales of dominating acoustic waves trapped inside the boundary-layer. It was estimated using Crocco's method for a compressible BL. Values of a dominant nondimensional frequency within the separation zone for cold and hot flow ranged $f \cdot \delta / U_\infty = 0.08$–$0.20$. Conversion to this nondimensional form removed the shift of the dominant physical frequency peak that occurred between various unit Reynolds numbers seen previously in [6]. The shift occurred as the result of different boundary-layer growth rates at each unit Reynolds number and the boundary-layer thickness at different streamwise locations. Since the boundary-layer acted as an acoustic wave guide (establishing a wavelength), as explained in [16], the dominant frequency of acoustic waves varied with the boundary-layer thickness. In Fig. 7, the "freestream" legend corresponds to a point in the dot matrix measured in the core flow far from the surface of the model, and "corner" represents the

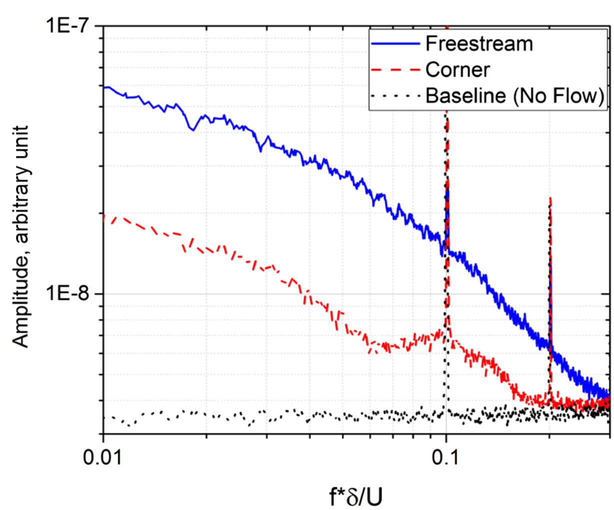

Fig. 7 SH deflection angle spectra ($Re_l \approx 3.5 \cdot 10^6$ m^{-1} and $T_0 = 300$ K).

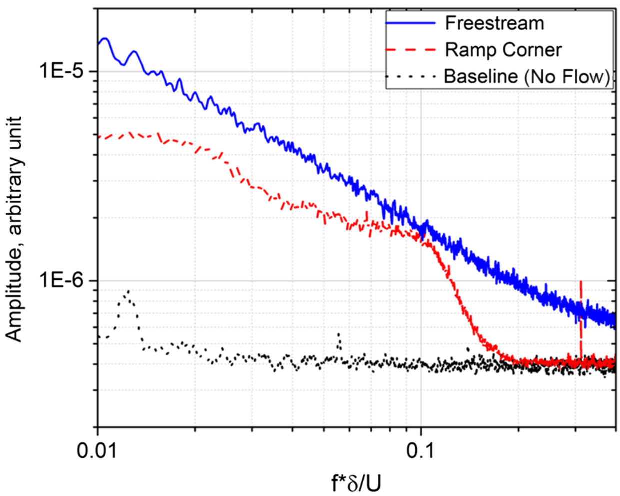

Fig. 8 Pressure perturbation spectra collected by PCB pressure sensor ($Re_l \approx 4.6 \cdot 10^6$ m^{-1} and $T_0 = 300$ K).

point closest to the corner (less than 1 mm above the surface and less than 1 mm in front of the ramp tip). The corner point indicates a clear reduction in the amplitude of oscillations from the freestream condition, with a local maximum existing in the spectra at a frequency of 0.1 shown in Fig. 7. The baseline measurements were also made without flow to show the noise floor of the system. Narrow, high-amplitude peaks observed in the data are attributed to a digitizing noise and have to be neglected in the analysis. As aerooptical effects are proportional to the freestream density, the signal-to-noise ratio of the SH sensor is higher for the cold flows than it is for the hot flows, as lower flow temperatures have a higher density that causes larger wavefront distortions and a larger signal without producing more noise. PCB™ (132 series) microsensors provided high-frequency pressure measurements along the model surface upstream of and within the corner separation zone. With a response frequency of up to 1 MHz and resolution of 7 Pa, these piezoelectric transducers are capable of detecting weak shocks and high-frequency perturbations impacting the sensor's diaphragm. Pressure data collected from the sensors provided reinforcing evidence of the dominant natural frequencies present in both high- and low-enthalpy flows. The spacing allowed for measurement of the flow pressure perturbations in the corner separation zone (CH3), near the flow separation point (CH2), and within the boundary-layer upstream (CH1). Schlieren images verified the location of separation and the existence of the separation zone near the corner. The sensors and their cables were carefully insulated to reduce vibrational noise from the model and electromagnetic noise from surrounding electronics. Figure 8 indicates a similar trend in the pressure data compared to the SH sensor results. Except for small spikes (due to electromagnetic (EM) noise, mainly in the baseline condition), the primary feature in the pressure frequency spectrum for the ramp corner signal is a reduction in perturbation amplitudes from the freestream case at frequencies above 0.1. The signal-to-noise ratio has a reasonably high value in most cases without the plasma generation. The noise level is extremely high during operation of the high-voltage, high-frequency power supply of the plasma generator due to the high sensitivity of piezoelectric sensors to EM noise. For the laser differential interferometer (LDI), a Melles–Griot linearly polarized He–Ne continuous-wave (CW) laser was used as the coherent light source. This setup is shown in Fig. 9. It passed through a quarter-wave plate with the ordinary and extraordinary axes aligned at 45 deg to the axis of polarization of the laser to produce a circularly polarized beam. The beam passed through a Wollaston prism to produce two orthogonally polarized beams of equal intensity, which diverged from each other at 2 deg. The Wollaston prism was at the focal point of a 1 m focal length lens such that the orthogonally polarized beams were parallel to each other. The beams then passed through the test section with one beam isolated from the flow disturbances and the other passing through the boundary-layer directly over the PCB inside the separation zone (CH3). The difference in density along the beam-integrated path, where the beam passed through the boundary-layer, introduced some new phase shift. An identical 1 m focal length lens focused the beams back to a point on another Wollaston prism. The overlapping beams were sent through a linear polarizer at 45 deg, and the beam was imaged onto a photodiode. The intensity measured by the photodiode depended on the phase difference between the orthogonally polarized beams. The constructive/destructive interference was governed by the phase shift introduced by the density perturbations in the flow. The limits of the system were noise introduced (vibrational, ambient light, etc.), the response time of the photodiode (generally very short, less than 1 μs), the beam diameter, and the measurement circuit used.

Measurements taken by the LDI further validated the SH wavefront sensor and PCB data. For comparison, baseline and freestream tests are shown in Fig. 10 to compare with measurements taken in the corner separation zone. It is evident that the measurements taken in the corner separation zone indicate the same peak dominant nondimensional frequency of 0.08 present in the SH wavefront sensor and PCB data (~60 kHz in dimensional frequency); perturbations existing near this frequency were the least damped from the freestream case. The low-frequency peak in the LDI baseline spectra was caused by facility mechanical vibrations.

Figure 11 presents the comparison of the spectra acquired by the three measurement methods from the near-corner area. These tests were carried out for a low Re_l case ($Re_l \approx 4.6 \cdot 10^6$ m^{-1}) in $T_0 =$ 300 K (low enthalpy) flow to ensure a laminar flow over the model. Spectra presented in Figs. 7–11 display the amplitude of perturbations in arbitrary units, which allow for the normalization of the PCB and LDI data for a convenient comparison with the SH data. The LDI results at higher Re_l suggest a turbulent flow, as evidenced by the similarity to the freestream case and a lack of any distinguishable dominant frequency (discussed later with the SH results). The flow configuration after the tunnel nozzle is a free round jet for which a turbulent shear layer is expected to develop at high Re_x. This turbulent shear layer masks the lower-amplitude fluctuations in the core flow, which causes issues for measuring the disturbances in the boundary-layer and separation zone. Both SH and LDI systems are path-integrated systems, and therefore they are unable to distinguish between disturbances that are in the separation zone and those that would exist in a turbulent shear layer. A major difference between SH and LDI systems is in the way the optical density is measured: a phase shift in beamwise direction for LDI, as SH measures disturbances occurring in the streamwise and wall-normal directions. The PCB pressure sensors provide pointwise measurements and are unaffected by this consideration. A focused LDI system may be able to resolve this issue, but the two-dimensional planar geometry of the compression ramp makes it difficult to implement in the region of interest. In Fig. 11, the frequency content

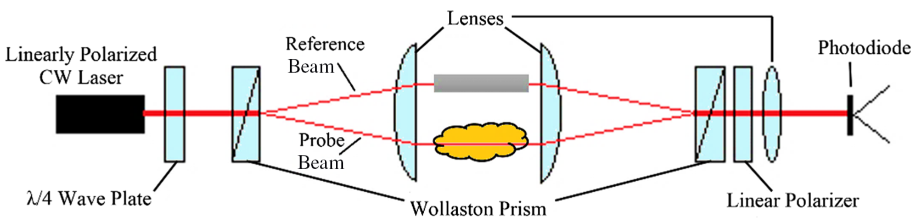

Fig. 9 Basic schematic of the laser differential interferometer.

Downloaded by UNIVERSITY OF NOTRE DAME on July 2, 2018 | http://arc.aiaa.org | DOI: 10.2514/1.J056576

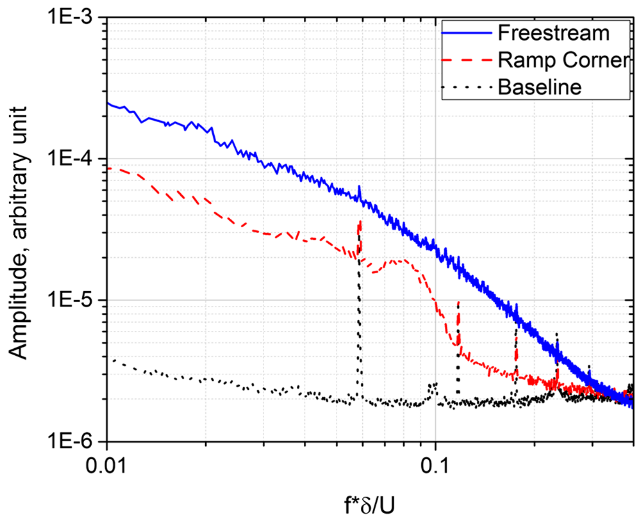

Fig. 10 Spectra of the LDI signal compared to the baseline with no flow ($Re_l \approx 4.6 \cdot 10^6$ m^{-1} and $T_0 = 300$ K).

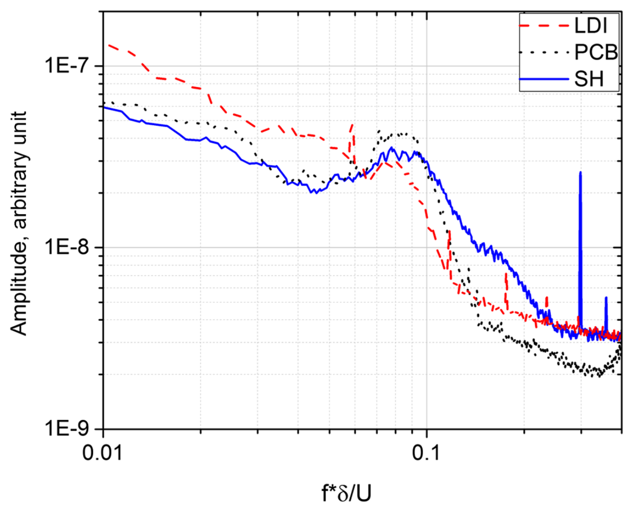

Fig. 11 Spectra comparison for SH wavefront sensor, pressure sensors PCB, and LDI.

of the LDI data below and above the dominant frequency differs from that obtained with the SH wavefront sensor. The LDI system is more susceptible to low-frequency external effects, such as optical table vibrations, than the SH system. These external effects along with higher sensitivity to disturbances in the shear layer contribute to the elevated amplitudes of the oscillations at frequencies below the dominant frequency as compared to the aerooptical data. The amplitude of the LDI frequency spectrum is slightly lower than that of the SH at frequencies higher than the dominant frequency, and the PCB data have an amplitude much lower than both. The PCB has a lower effective level of the noise threshold and is collecting data at a single point, while the two optical methods are path integrated. Once plasma actuators are implemented, the use of pressure sensors becomes problematic due to the high level of electromagnetic noise generated by the discharge. Thus, in the case of characterizing the fluctuations for the planar hypersonic compression ramp, the SH wavefront sensor has shown to be the most effective tool for data collection due to its high temporal resolution, ability to collect spatially resolved data over a region, and its relative insensitivity to perturbations present in the freestream outside of the region of interest.

Each of the diagnostic tools poses sources of inaccuracy in the results. For the electric parameters during plasma actuation, an accuracy of electrical probes is $\pm 1\%$ for Pearson™ current probes and $\pm 2\%$ for LeCroy™ PPE20KV high-voltage probes. For the SH wavefront sensor, some amount of uncertainty rests in the wall-normal distance of the dot matrix from the model; this spatial uncertainty is estimated to be < 0.1 mm ($< 10\%$ of δ). The temporal resolution of the SH system is limited by the camera system, a Phantom V1611 high-speed camera measuring at 531,645 Hz. High-frequency pressure measurements taken by factory-calibrated PCB™ include high-pass filtering at 11 kHz and a resonant frequency greater than 1 MHz. The flow oscillatory frequencies of interest in this study exist above the low-frequency response and below the sensor's resonant frequency. The LDI is a spanwise integrating measurement, which can detect up to $\pm\lambda/4$ optical path difference without introducing phase ambiguity on the interference sine curve. Most disturbances for the tested conditions are within $\pm\lambda/8$, which is within the highly linear region of the interference curve. Because of the spanwise integration, it is difficult to quantify the uncertainty. It is within reason to use an estimated error of $\pm 5\%$ while the measurement remains within the linear portion of the sine curve. It is mostly the frequency content of the data that is of interest to this study. How all of these uncertainties transfer into the frequency domain is not obvious. However, all sensors employed have a much higher-frequency limit than the frequency content of the flow. With this in mind, it is within reason to estimate the uncertainty of the frequency content to be $\pm 2\%$ in determination of the dominant frequency.

III. Experimental Results

A. Boundary-Layer Transition

Initial characterization of the flow by three methods in this study has shown the SH wavefront sensor to be the most suitable tool to analyze the state of the BL, including dominant frequencies within the flow spectra, in the case of electromagnetic noise. The flow perturbations can be further analyzed at individual regions within the flow. Figure 12 shows the field of measurements performed by the Shark–Hartman sensor. There are four lines with ten points in each. Points are masked by the model ramp in the corner. The distance between the points in the X and Y directions is 1.2 mm.

Figure 13 shows the nondimensional frequency spectrum of the flow along two line profiles at high and low Re_l in low-enthalpy ($T_0 = 300$ K) flow. The spectra in Figs. 13b and 13d show that a significant amount of low-frequency perturbations exists in the freestream for low and high Re_l flows, which grow as they travel downstream. It is apparent that at low Re_l (laminar flow) the line profile closest to the wall (4.4–4.10) exhibits higher-amplitude fluctuations than in the freestream in the lower-frequency bands, which could indicate that initial perturbations in the freestream experience some growth in the flat-plate boundary-layer. Additionally, a damping effect in the amplitude of fluctuations is seen as the flow approaches the corner of the ramp (Fig. 13a). This effect appears strongest in the low-frequency band of oscillations, which may have originated in the freestream, grows along the flat plate, and then begins to damp in the region of separation. This effect is not noticeable far from the wall in Fig. 13b. It is also important to note that point 1.1 is located downstream of the compression shock, which accounts for the increase in amplitude from points 1.10 and 1.6. At high Re_l, the amplitude of disturbances increases as the flow travels downstream and does not have distinguishable flow features in the frequency domain. A steady decay in the fluctuations, coupled with a lack of any dominant peaks at locations near and far from the wall, shown in Figs. 13c and 13d, indicates that a transitional/turbulent flow exists throughout the near-wall flowfield at this high of Re_l. Discrete peaks in the spectra in Figs. 13–15 represent a source of digitizing noise and its harmonics. These appear as a result of quantization during the data processing and do not correspond to any physical signal in the flow.

The same measurements were performed for high-enthalpy flows ($T_0 = 1238$ and 835 K), with relatively low and high Re_l cases. In this situation, the line profile along the wall (Figs. 14a and 14c) indicates the presence of a raised peak in the spectra occurring downstream (in the ramp corner). Figure 14c indicates a damping of fluctuations near the ramp corner at frequencies below 0.09 and an amplification of higher frequencies. Far from the wall, the downstream locations exhibit the largest fluctuations with few

Downloaded by UNIVERSITY OF NOTRE DAME on July 2, 2018 | http://arc.aiaa.org | DOI: 10.2514/1.J056576

Downloaded by UNIVERSITY OF NOTRE DAME on July 2, 2018 | http://arc.aiaa.org | DOI: 10.2514/1.J056576

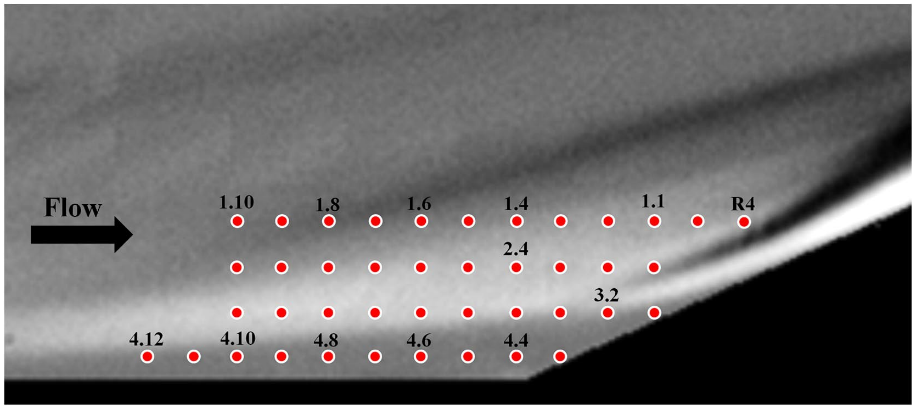

Fig. 12 Dot matrix of SH measurement locations combined with a typical schlieren image; the distance is 1.2 mm between points.

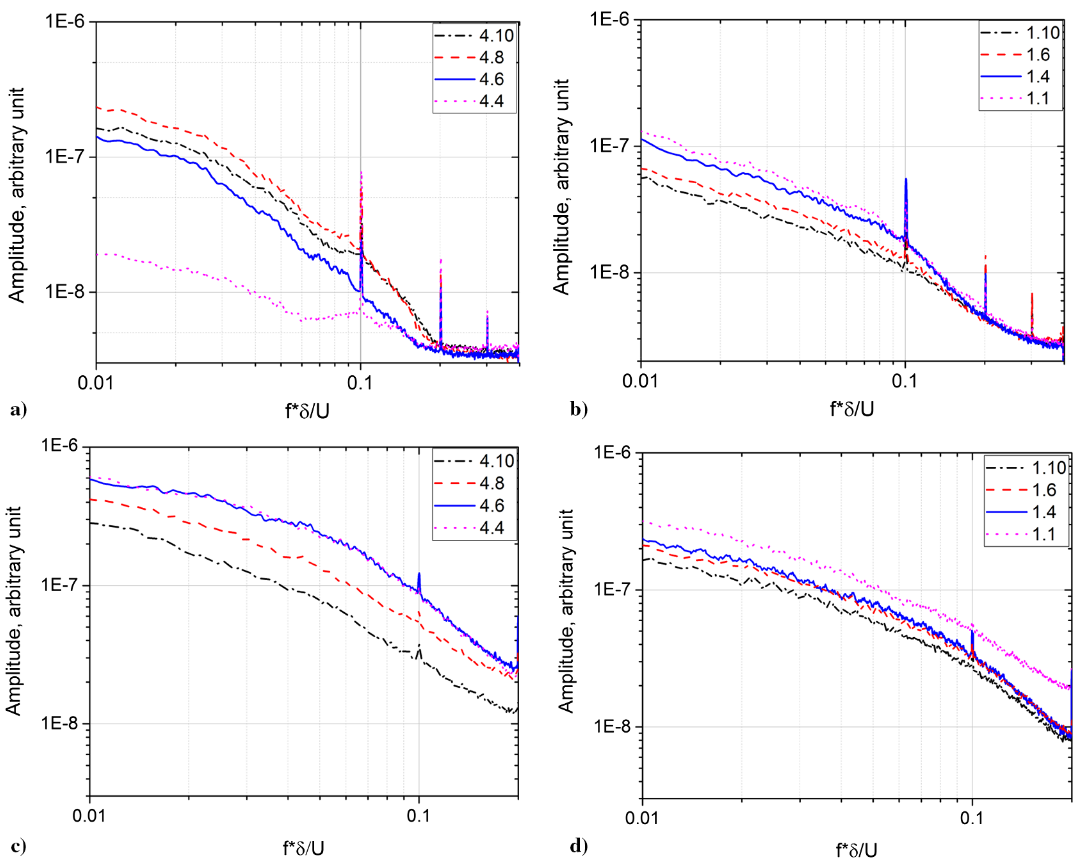

Fig. 13 Spectrum of SH data for low-enthalpy flow ($T_0 = 300$ K): a) and b) $Re_l \approx 3.5 \cdot 10^6$ m^{-1} and c) and d) $Re_l \approx 1.3 \cdot 10^7$ m^{-1}.

distinguishable features in the frequency domain, similar to the low-enthalpy flow cases.

The boundary-layer conditions were characterized based on the features of flow perturbation spectra. Figure 15 presents the data in terms of the PSD, which was defined as $PSD = \breve{\rho}^2 \cdot f(\text{in Hz}^{-1})$, where $\breve{\rho}$ is a wall-normal component of the deflection angle measured by the SH sensor in arbitrary units. However, one should be careful when comparing the data from the SH sensor, which measures spanwise-integrated density perturbations [20,37], to the local pressure sensor data. Nevertheless, as the density and the pressure are related via the equation of state, the results can be compared qualitatively. The data are shown for three cases: 1) $P_0 = 5.5$ bar and $Re_l \approx 1.3 \cdot 10^7$ m^{-1}, 2) $P_0 = 1.5$ bar and $Re_l \approx 3.5 \cdot 10^6$ m^{-1}, and 3) $P_0 = 1.5$ bar and $Re_l \approx 4.6 \cdot 10^5$ m^{-1} (high enthalpy). Data are shown for freestream point 1.10 (see Fig. 12); close to the ramp point 1.1; in the boundary-layer point 4.9, which is far upstream from separation zone; and in the separation zone point 4.4. Note the increase of the baseline with frequency indicates that the system is close to the sensitivity limit.

In case 1, the level of flow perturbations is high compared to other cases. The PSD could be attributed to the turbulent flow in the freestream (point 1.10) and in the BL (point 4.9). The intensity increases further near the ramp due to effect of the separation-related shock. The amplitude of perturbations in the separation zone is high with dominance at relatively low frequencies $f < 100$ kHz. In case 2, the freestream spectra look similar to case 1, except for the amplitude, which is approximately ρ^2 times lower. Contrary to case 1, the intensity of perturbations rises in the boundary-layer but is significantly damped in the separation zone. At the lowest Re_l in case 3, the freestream perturbations are lower than the detection threshold, demonstrating a significant rise on the ramp behind the shock wave and in the separation zone. Based on the nondimensional frequency spectrum at location 4.9, the boundary-layer is laminar. The nondimensional frequency spectrum at location 4.4 indicates the

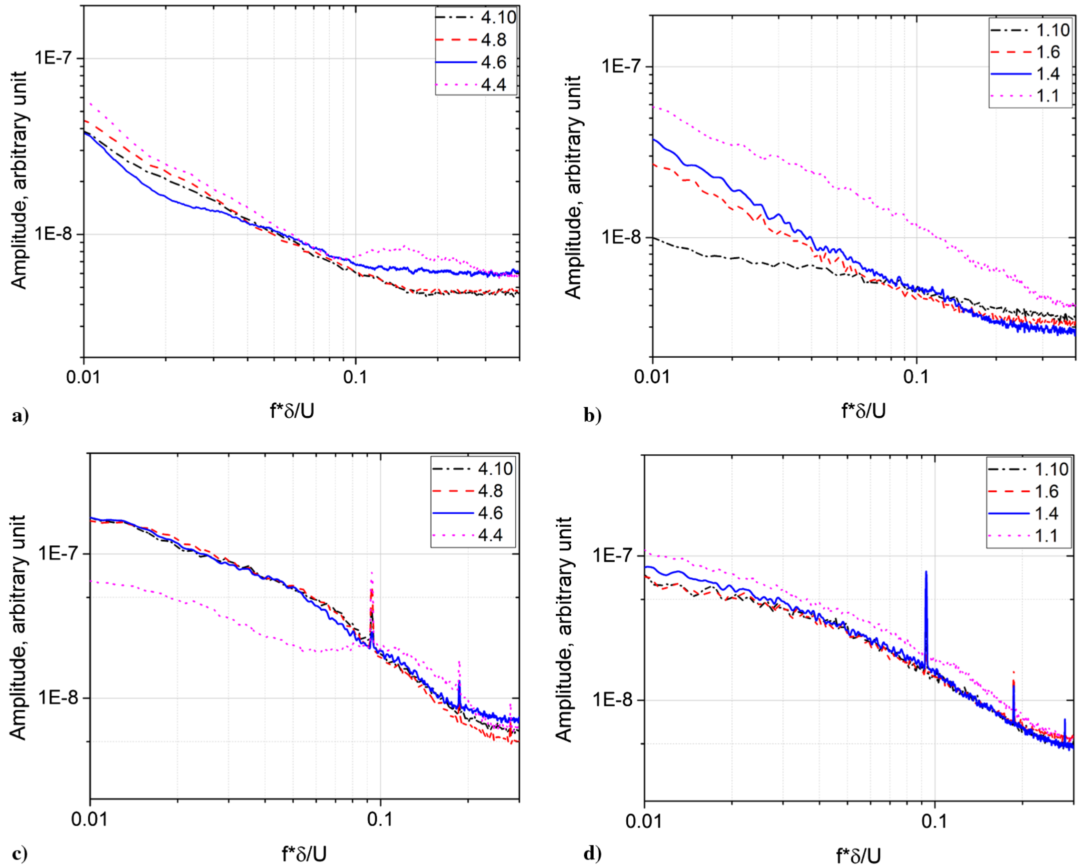

Fig. 14 Spectrum of SH data for high-enthalpy flow: a) and b) $Re_l \approx 4.6 \cdot 10^5\ \mathrm{m}^{-1}$ ($T_0 = 1238$ K) and c) and d) $Re_l \approx 1.6 \cdot 10^6\ \mathrm{m}^{-1}$ ($T_0 = 835$ K).

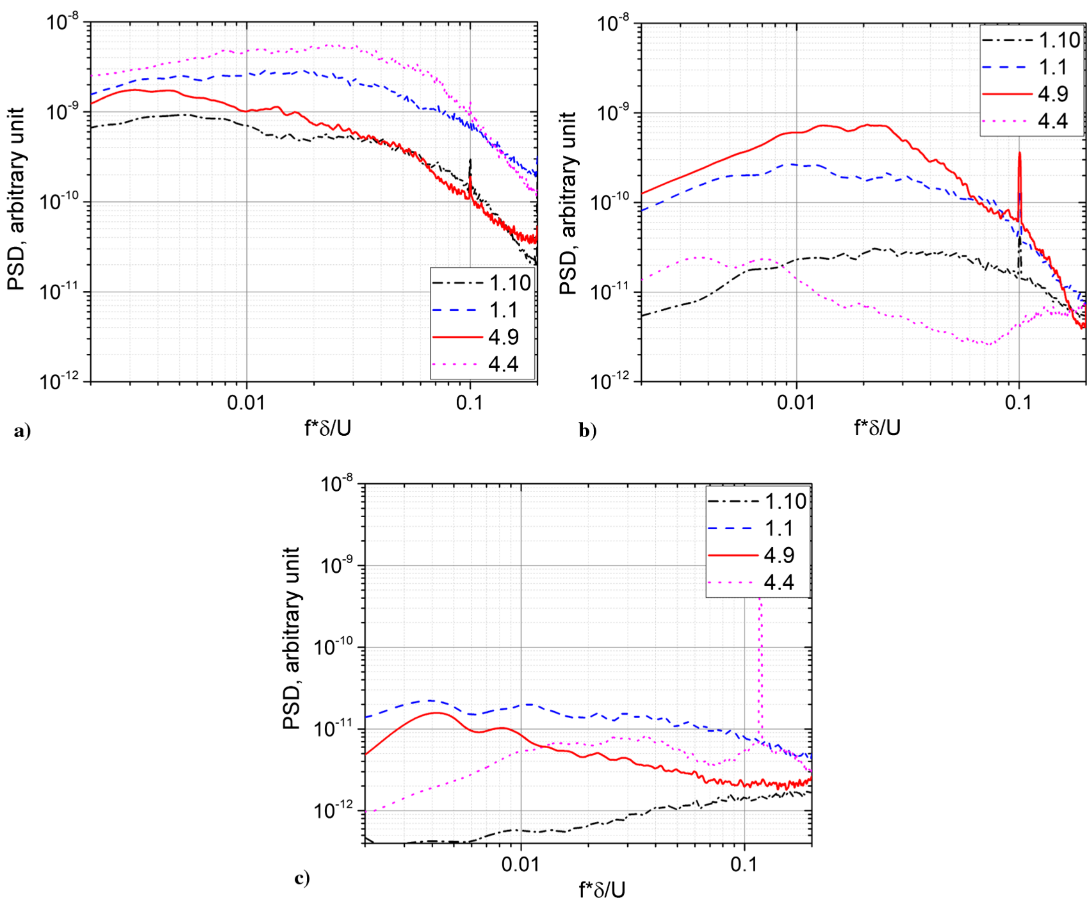

Fig. 15 Power spectral density of flow perturbations for a) $P_0 = 5.5$ bar and $Re_l \approx 1.3 \cdot 10^7\ \mathrm{m}^{-1}$, b) $P_0 = 1.5$ bar and $Re_l \approx 3.5 \cdot 10^6\ \mathrm{m}^{-1}$, and c) $P_0 = 1.5$ bar and $Re_l \approx 4.6 \cdot 10^5\ \mathrm{m}^{-1}$.

Downloaded by UNIVERSITY OF NOTRE DAME on July 2, 2018 | http://arc.aiaa.org | DOI: 10.2514/1.J056576

presence of dominant frequencies with increased magnitude, which could be attributed to the development of the acoustic instabilities. Based on the criteria described in [13,14],

$$\xi_M = \frac{\beta Re_l^{1/4}}{(M_\infty^2 - 1)^{1/4}} \tag{3}$$

is equal to $\xi_M \approx 3$, and this mode should experience separation with distorted friction. The criteria (3) are valid for the laminar BL, predicting a secondary separation at the increasing value of Re_l. In the current configuration and at a high level of initial disturbances in the flow, the increase of Re_l does not cause secondary separation but leads to the flow transition.

B. Flow Disturbances at Low Re_l

Further analysis of the SH data is performed for results collected for low- and high-enthalpy tests at the lowest Re_l conditions possible for the facility in order to maintain laminar flow. These conditions correspond to $Re_l \approx 2.7 \cdot 10^6\ \mathrm{m}^{-1}$ for the low-enthalpy flow and $Re_l \approx 4.6 \cdot 10^5\ \mathrm{m}^{-1}$ for the high-enthalpy flow. These results reinforce previous characterization of the perturbations present in the hypersonic boundary-layer [5]. The analysis provided shows that the same dominant natural nondimensional frequency is detected as it is presented in Fig. 16. The locations of points 4.12–4.4 (two adjacent points are 1.2 mm apart) in Figs. 16a and 16b correspond to locations in the flowfield where Shack–Hartmann measurements were taken. The dominant frequency appears to be significantly higher for the high-enthalpy tests. This observation can be explained by two effects. The more dominant effect is due to a decrease in Re_l during the high-enthalpy tests. The second is due to the cooling effect of the wall on the flow, which corresponds to a reduction in boundary-layer growth. Studies have shown that the cold wall constrains the growth of first mode (Tollmien–Schlichting) waves and accelerates the growth of second mode waves in the boundary-layer [16,38]. Since arc heating during high-enthalpy tests greatly increases the flow temperature in relation to the wall, heat transfer exists between the flow and wall. In the low-enthalpy tests, the wall is nearly adiabatic, whereas the high-enthalpy tests do not exhibit an adiabatic behavior with the wall due to the short run time. The dominant disturbances for low Re_l flows, which are believed to have a laminar boundary-layer, are acoustic waves. Recall that the boundary-layer acts as a waveguide and traps acoustic waves in the boundary-layer [16]. This results in a relation between the boundary-layer thickness and the wavelength of the trapped acoustic waves; a thinner boundary-layer possesses higher-frequency acoustic waves. However, the gas temperature affects the sonic velocity. As a result, the high-enthalpy flow boundary-layer will have a higher dominant frequency of perturbations, which is shown in Fig. 16. This pathway, however, is difficult to detect due to complexity of changes in the velocity, density, pressure, and wall/gas temperature. The dominant frequency in the low-enthalpy flow corresponds to $f = 55$ kHz at $Re_l \approx 2.7 \cdot 10^6\ \mathrm{m}^{-1}$, and in the high-enthalpy flow, it is about $f = 110$ kHz at $Re_l \approx 4.6 \cdot 10^5\ \mathrm{m}^{-1}$. Both values are about consistent with the estimated thickness of the BL. From Fig. 16, the points measured closer to the corner position indicate higher-frequency amplitudes up to some distance (4.7), and then the signal is damped similar to one shown in Fig. 15.

C. Plasma Actuation

With the dominant natural frequencies present in the boundary-layer determined under these test conditions, it was then possible to study the effect of pulse-repetitive SCD operation on the spectra of flow perturbations in and near the corner separation zone. The deflection-angle spectra obtained using the high-speed SH wavefront sensor were analyzed at the locations indicated in Fig. 12. Note that the use of the pressure sensors was challenging under these conditions due to a high level of the electromagnetic noise associated with the plasma operation. Early results showed [5] that SCD operation affected the spectra only slightly if the repetition frequency was less than the dominant frequency of flow perturbations, $F_1 = 55$–70 kHz. Operating at a frequency greater than F_1 produced significant changes in the spectra of disturbances.

As mentioned previously, the wavefront sensor measures horizontal or streamwise (X) and vertical or wall-normal (Y) components of the deflection angle. The deflection angle is simply the gradient to the resulted aerooptical wavefront. Isotropic flows generally display close to equal magnitudes of the wavefront gradient in the horizontal and vertical directions. The near-wall flow considered in this study is expected to have larger magnitudes of deflection angles in the wall-normal (Y) direction compared to the streamwise (X) direction due to the larger density gradients in the wall-normal direction. This in turn amplifies the effect that the plasma has on exciting the higher-frequency disturbances and results in larger magnitudes of deflection angles.

The effect of pulsed plasma actuation at $F = 100\ \mathrm{kHz} > F_1$ repetition rate on the spectra of flow perturbations is shown in Fig. 17. Points of interest include 4.7 and 4.4 along the model wall leading up to the corner, where a small plasma effect appears to exist. Higher-amplitude fluctuations during plasma actuation at location 2.4 indicate a Y shift of the boundary of separation zone and a modification of the separation zone dimensions. Point R4, located near the root part of the shock generated by the ramp shows a significant response to the plasma actuation. This effect, shown in Fig. 17d, exists as an amplification of flow disturbances for all observed frequencies. Point R4 is approximately where the boundary-layer reattaches to the ramp, and this location is often the location of transition from a laminar to turbulent boundary-layer [11]. The resulting amplification of flow perturbations at R4 due to the operation of the SCD actuators is $A/A_0 = 2$–8. At the same time, the effect is negligibly small in the BL and inside of the separation area.

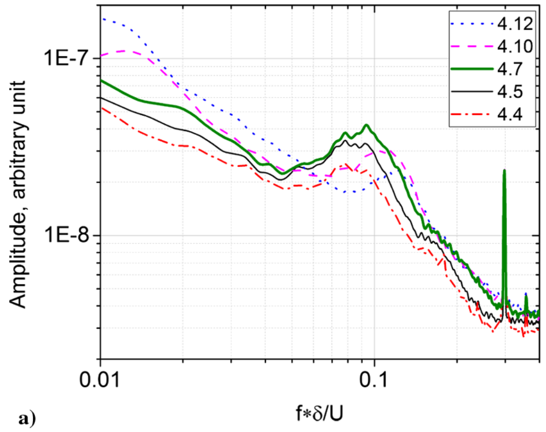

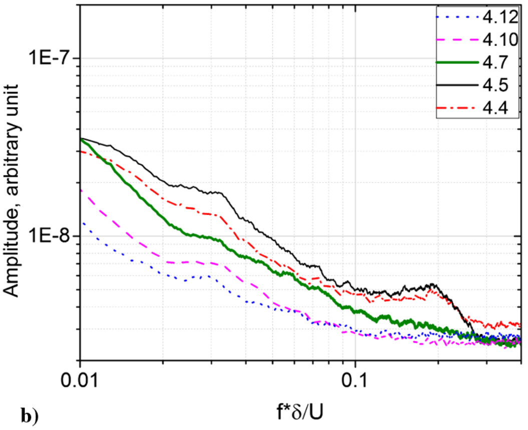

Fig. 16 Spectra collected by SH wavefront sensor from a) low-enthalpy test ($T_0 = 300$ K and $Re_l \approx 2.7 \cdot 10^6\ \mathrm{m}^{-1}$) and b) high-enthalpy test ($T_0 = 1238$ K and $Re_l \approx 4.6 \cdot 10^5\ \mathrm{m}^{-1}$).

Downloaded by UNIVERSITY OF NOTRE DAME on July 2, 2018 | http://arc.aiaa.org | DOI: 10.2514/1.J056576

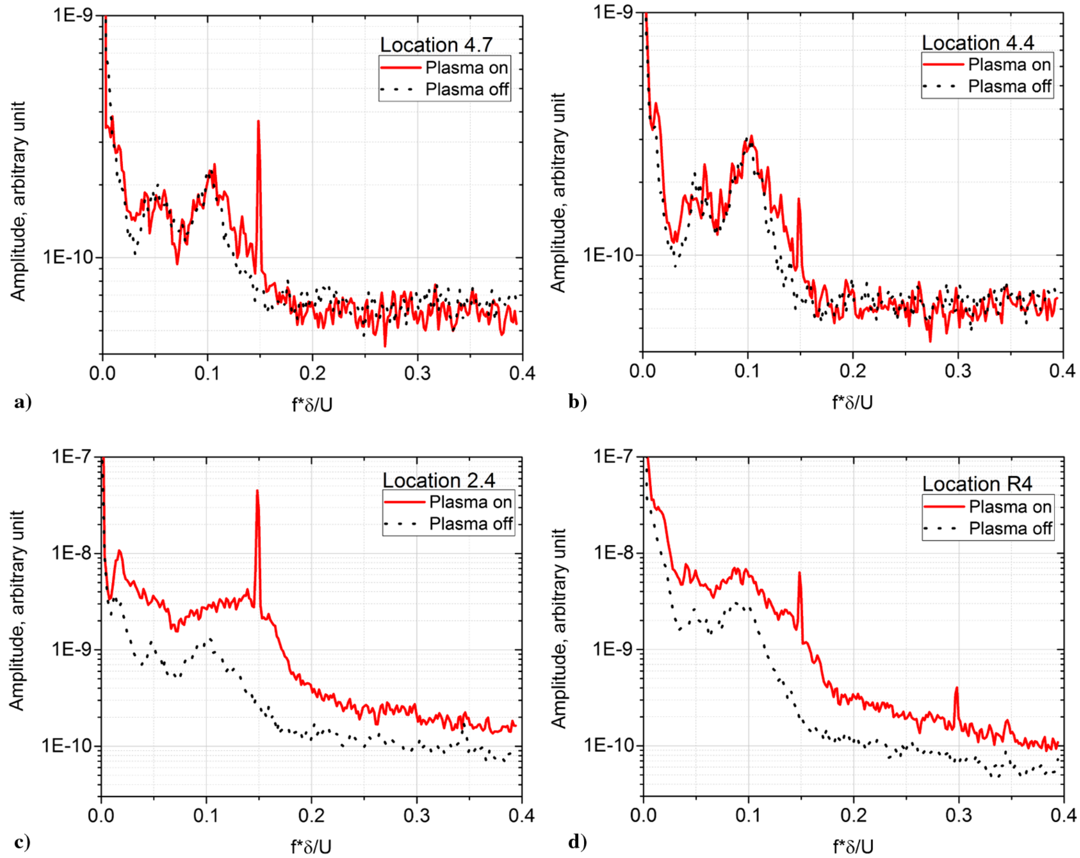

Fig. 17 Spectra of SH data, plasma excitation $f = 100$ kHz: locations a) 4.7, b) 4.4, c) 2.4, and d) R4 ($T_0 = 300$ K and $Re_l \approx 2.7 \cdot 10^6$ m^{-1}).

Downloaded by UNIVERSITY OF NOTRE DAME on July 2, 2018 | http://arc.aiaa.org | DOI: 10.2514/1.J056576

IV. Discussion

In addition to the spectra of density oscillations, the SH method provides information on the spatial-temporal distribution of flow parameters and, to some extent, on a causality of gas perturbations. As was mentioned previously, the data on the optical density-related oscillations are acquired at multiple discrete lines of observation; see Fig. 12. Particularly, the data postprocessing poses the correlation function and the coherence between any pair of time series. The correlation function $C(\tau)$ between two signals indicates their proximity in a time domain, frequently allowing a simple calculation of a time delay and a perturbation velocity in a physical space, while a calculation of the coherence function $\Gamma_{xy}(f)$ allows recognition of congruence of two signals in a spectral (Fourier) space [39–41]. Both correlation and coherence functions are normalized to 1. The normalized correlation function $C(\tau)$ is defined as

$$C(\tau) = \frac{\int_{-\infty}^{\infty} f(t) \cdot g(t+\tau)\, \mathrm{d}t}{\sqrt{\int_{-\infty}^{\infty} f^2(t) \cdot g^2(t+\tau)\, \mathrm{d}t}} \tag{4}$$

where $f(t)$ and $g(t)$ are the two signals of the same length compared. Additionally, the normalized coherence function $\Gamma(f)$ is given by the equation

$$\Gamma_{xy}(f) = \frac{|P_{xy}(f)|^2}{P_{xx}(f)P_{yy}(f)} \tag{5}$$

where P_{xy} is the cross-power spectral density of the two signals, $\hat{x}$ and $\hat{y}$; see Eqs. (1) and (2). P_{xx} and P_{yy} are the power spectral densities of x and y.

Figure 18 demonstrates the result of a correlation analysis of SH signals in the freestream (a) and in the BL [(b) and (c)]. In the freestream, the most upstream line, point 1.10 was chosen as the base for comparison. The amplitude of the correlation decreased, and the time delay increased with the distance between calculated SH positions. Based on the measured data, the flow velocity over the model surface was calculated to be $v = 670 \pm 30$ m/s for $T_0 = 293$ K and $v = 1100 \pm 100$ m/s for $T_0 = 835$ K. These values are a bit lower than the flow velocity at the nozzle exit (Table 1), which can be explained by the presence of a series of shock waves generated in the flow over the length of the model. As is shown in Fig. 18b, the correlation of disturbances in a pair of surrounding areas is similar for most points. The exception is only for two points (one correlation) located closest to the corner zone, marked as “4.4 & 4.3.” For this area, the correlation was observed to have a lower amplitude and a small delay time, $\tau < 1$ μs, indicating a reduced length of the separation zone. In Fig. 20c, taken for a lower unit Reynolds number $Re_l = 4.6 \cdot 10^6$ m^{-1}, four measuring lines (three correlations) are attributed to the separation zone. This observation further proves the flow modes characterization, discussed in Sec. III.

Based on the coherence calculation, Fig. 19, the SH signal possesses a high magnitude in a wide range of frequencies if both signals are taken from the BL before separation, points 1.9 to 1.10 and 4.6 to 4.7. In the case in which the signals are compared near the separation line, point 4.4 to point 4.5, a loss of coherence is observed at selected frequencies, which is quite consistent with the dominant frequency of the flow disturbances. In the separation zone, the signals are coherent at frequencies below 50 kHz, corresponding to a dimensionless frequency of 0.066.

One more conclusion should be expressed on the adequacy of the spanwise-integrated measurements performed with the SH sensor to pointwise surface data taken with the pressure sensors. Figure 20 shows the normalized correlation function between the X component of the SH signal and the pressure sensor PCB CH3 located in the corner. The two signals are well correlated, with a time difference $\tau = -29$ μs, which may be attributed to some distance between the sensor location and a relatively low flow velocity in the separation zone. It should be noted that the correlation between two different pressure sensors has a much lower amplitude than between SH and

Downloaded by UNIVERSITY OF NOTRE DAME on July 2, 2018 | http://arc.aiaa.org | DOI: 10.2514/1.J056576

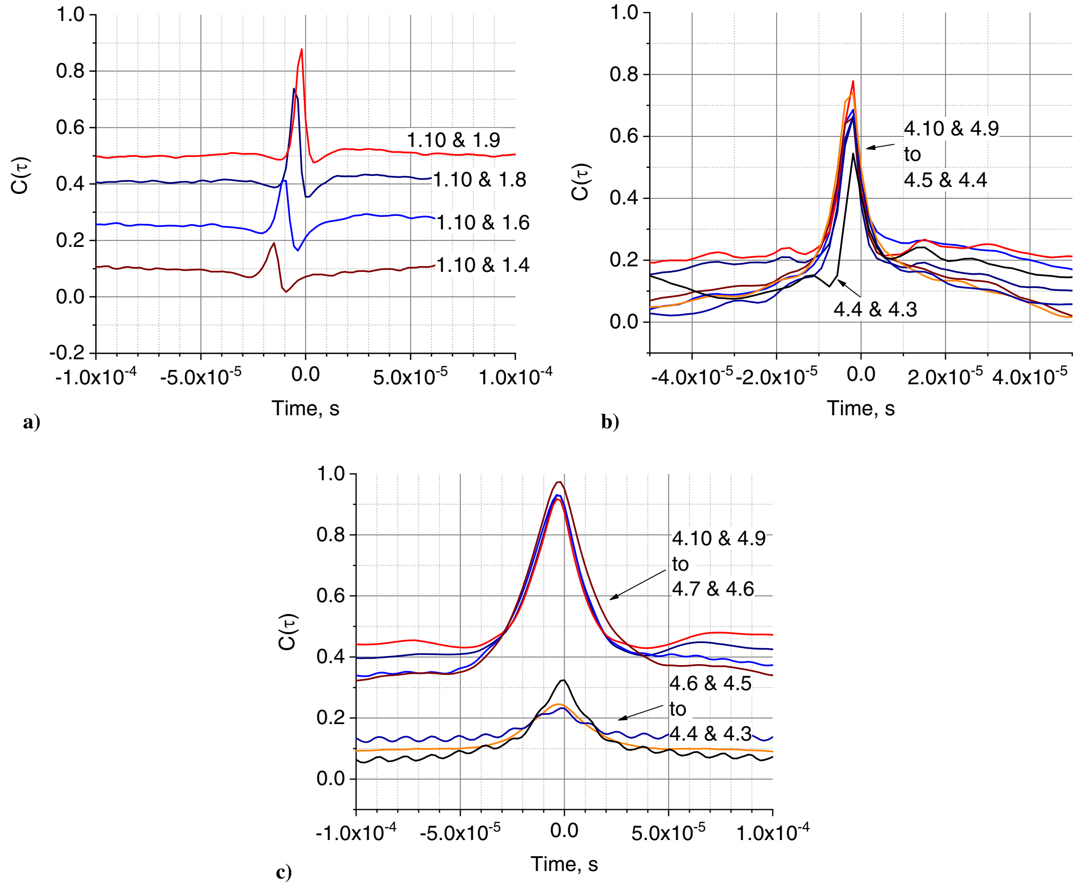

Fig. 18 Correlation of X component of SH signal in a) freestream and b) and c) near-wall area (BL and separation zone). a) and b) $Re_l = 1.3 \cdot 10^7$ m^{-1} ($P_0 = 5.5$ bar), and c) $Re_l = 4.6 \cdot 10^6$ m^{-1} ($P_0 = 1.9$ bar).

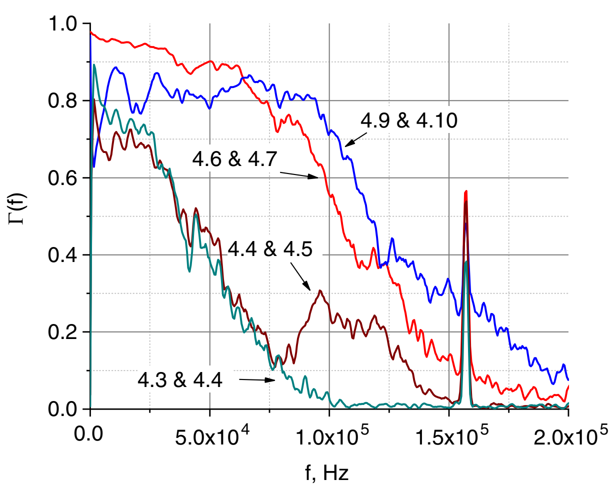

Fig. 19 Coherence of SH signals in BL and separation zone. $Re_l = 4.6 \cdot 10^6$ m^{-1} ($P_0 = 1.9$ bar).

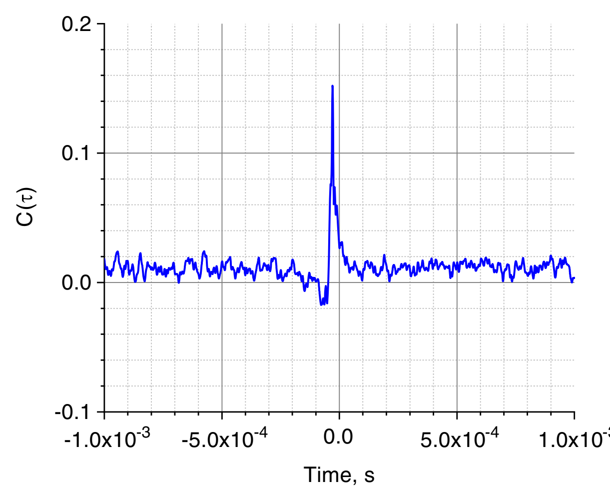

Fig. 20 Correlation function of SH optical sensor located in the corner separation zone and the pressure sensor PCB 3.

PCB sensors located in a close proximity to each other. This is caused by a significant difference in the pressure sensor location in both the spanwise and the streamwise directions.

The characterization of flow regime (laminar, transitional, and turbulent) of the experimental flowfield is an important factor to discuss as well. Primarily of concern, the state of the flow has been shown to affect both the size of separation and frequency of oscillations of separation-related shocks [10,42–44]. At higher Re_l, the separation zone often diminishes or disappears. The spectra in Figs. 13–15 indicate that flow may contain turbulent structures within the freestream (1.10–1.1) and even near the ramp corner in the highest tested Re_l regimes. In addition, the damping effect on the oscillations caused by the separation is no longer seen in these highest Re_l cases. These spectral results give evidence toward the reduction of the corner separation due to the onset of transition. Previous studies have shown that there is some dependence of transition Re_x on both the Mach number and Re_l in various conditions [45,46]. Tunnel noise, which may result from acoustic waves radiating from the nozzle walls, has been shown to have a significant effect on reducing the transition Re_x [45]. For instance, an experiment by Coles [47] identified transition on a flat plate at $Re_x = 1 \cdot 10^6$ in a noisy tunnel under similar flow conditions. These support the notion that transition occurred at the highest tested Re_l cases discussed within.

Downloaded by UNIVERSITY OF NOTRE DAME on July 2, 2018 | http://arc.aiaa.org | DOI: 10.2514/1.J056576

V. Conclusions

A canonic geometrical configuration has been tested in $M = 4.5$ high-enthalpy flow consisting of a flat surface at zero angle of attack and a compression ramp with an inclination of 30 deg in order to identify the flow pattern in the vicinity of the corner separation zone that is characterized by the appearance of an oblique shock wave originating from the wedge of the separation zone. Such a configuration models the geometry of a planar hypersonic compression ramp well. The spectra of flow pressure perturbations were gathered from surface-mounted pressure sensors and compared to the flow density perturbations measured nonintrusively by Laser differential interferometry (LDI) and a high-frequency Shack–Hartmann (SH) sensor. These optical methods have shown to be especially useful in this environment, as they are nonintrusive to the flow and capable of obtaining spatially and temporally resolved data. Of the optical methods employed in this study, SH wavefront sensing has been shown to be the best due to its ability to collect temporally resolved, density-related deflection angles in both streamwise and wall-normal directions presenting their spatial distribution in the flowfield. It is also relatively insensitive to vibrations and electromagnetic noise and easier to employ compared to other optical diagnostics. The LDI provides high-frequency measurements similar to the SH wavefront sensor, but instead it measures phase differences in the spanwise direction, and it is not ideal for flows with shear layers outside the region of interest, typical for open jet facilities. While frequency data from these optical methods are the result of measurements of the density fluctuations within the flow, pressure perturbations at the surface can also be measured by surface-mounted sensors. Each of these methods detected the same dominant nondimensional frequency in the boundary-layer/separation zone and therefore reinforces the results obtained via each other method.

The dominant frequency in the boundary-layer was detected in the range of $f = 55$–70 kHz in cold flow ($T_0 = 300$ K) and $f = 90$–120 kHz in hot flow ($T_0 > 800$ K). There was a shift to lower frequencies as the boundary-layer approached the corner separation zone due to the increasing thickness of the boundary-layer. The increase in the boundary-layer thickness increased the wavelength of the trapped acoustic waves, thus decreasing the frequency. In terms of the dimensionless frequency, the peak was located near $f \cdot \delta / U_\infty = 0.1$ in cold flow. With further characterization performed by the SH wavefront sensor, higher levels of disturbances occurred at higher Re_l in the boundary-layer (BL) and separation zone. In such cases, flow disturbances within the main flow affect the BL and can lead to a bypass transition to turbulence along the model. Only in the lowest Re_l cases does the presence of laminar flow allow for the detection of trapped acoustic instabilities in the separation zone. For most intermediate Re_l cases, the flow is characterized as transitional.

An attempt to control the flowfield pattern in the compression configuration of the flow has been performed with application of a highly transient plasma generator arranged midway between the test model leading edge and the compression ramp. The generation of a constricted plasma in a low-density gas, typical for high-speed boundary-layers, is of utmost importance in actually being able to affect the flow structures on the appropriate time scales. The shallow cavity discharge (SCD) has been shown to fit this need. The specific geometry of the SCD used, a one-dimensional array of plasma elements in the spanwise direction with individual control of each element, has demonstrated its effectiveness in exciting high-frequency disturbances within the flow. These tests have also demonstrated the feasibility of high repetition rate plasma operation in low-density, high-speed flows. The provided analysis of the data has led to a conclusion that hypersonic boundary-layers are sensitive to highly transient plasmas. Active tripping of the boundary-layer by electrical discharges can be done for a wide range of flow conditions so long as the forcing frequency is higher than the dominant frequency of perturbations present in the boundary-layer; $f > F_1$. It was also shown that plasma actuation has a significant effect at multiple points in the flowfield, especially near the area of flow separation/reattachment. In this region of the flowfield, the magnitude of the flow perturbations was increased two to eight times, which suggests plasma actuation is a robust technique to increase the level of perturbations in shear layer near the flow reattachment in a compression ramp configuration.

Acknowledgments

The current Paper is supported by the FlowPAC Institute at the University of Notre Dame. The authors would like to thank Nicholas DeLucca for his invaluable help in setting up and collecting data with the SH wavefront sensor. The authors express their gratitude to Alexander Fedorov for multiple discussions on the subject.

References

[1] Kriegseis, J., Simon, B., and Grundmann, S., "Towards In-Flight Applications? A Review on Dielectric Barrier Discharge-Based Boundary-Layer Control," *Applied Mechanics Reviews*, Vol. 68, No. 2, 2016, pp. 1–41.
doi:10.1115/1.4033570

[2] Im, S., Do, H., and Cappelli, M., "The Manipulation of an Unstarting Supersonic Flow by Plasma Actuator," *Journal of Applied Physics D: Applied Physics*, Vol. 45, No. 48, 2012, pp. 1–8.
doi:10.1088/0022-3727/45/48/485202

[3] Shin, J., "A Study of Direct-Current Surface Discharge Plasma for a Mach 3 Supersonic Flow Control," Ph.D. Dissertation, Dept. of Aerospace Engineering and Engineering Mechanics, Univ. of Texas at Austin, Austin, TX, 2007.

[4] Lin, K., and Yan, H., "Numerical Simulation of Supersonic Shear Layer with Plasma Actuator," *Procedia Engineering*, Vol. 126, No. 1, 2015, pp. 44–48.
doi:10.1016/j.proeng.2015.11.175

[5] Houpt, A., Hedlund, B., Gordeyev, S., Juliano, T., and Leonov, S., "Transient Plasma Impact on Spectra of Flow Disturbances in a Corner Separation Zone at Mach 4.5," AIAA Paper 2016-3807, 2016.
doi:10.2514/6.2016-4304

[6] Hedlund, B., Houpt, A., Gordeyev, S., and Leonov, S., "Measurement of Plasma Induced Flow Perturbations Affecting a Mach 4.5 Corner Separation Zone," AIAA Paper 2017-0154, 2017.
doi:10.2514/6.2017-0154

[7] Berry, S. A., Nowak, R. J., and Horvath, T. J., "Boundary Layer Control for Hypersonic Airbreathing Vehicles," AIAA Paper 2004-2246, 2004.
doi:10.2514/6.2004-2246

[8] Schneider, S., "Effects of Roughness on Hypersonic Boundary-Layer Transition," *Journal of Spacecraft and Rockets*, Vol. 45, No. 2, 2008, pp. 193–209.
doi:10.2514/1.29713

[9] Reshotko, E., and Tumin, A., "Role of Transient Growth in Roughness-Induced Transition," *AIAA Journal*, Vol. 42, No. 4, 2004, pp. 766–770.
doi:10.2514/1.9558

[10] Wu, Y., Yi, S., He, L., Chen, Z., and Zhu, Y., "Flow Visualization of Mach 3 Compression Ramp with Different Upstream Boundary Layers," *Journal of Visualization*, Vol. 18, No. 4, 2015, pp. 631–644.
doi:10.1007/s12650-014-0255-9

[11] Egorov, I., Fedorov, A., Novikov, A., and Soudakov, V., "Direct Numerical Simulation of Supersonic Boundary-Layer Stabilization by Porous Coatings," AIAA Paper 2007-948, 2007.
doi:10.2514/6.2007-948

[12] Egorov, I., Novikov, A., and Fedorov, A., "Numerical Modeling of the Disturbances of the Separated Flow in a Rounded Compression Corner," *Fluid Dynamics*, Vol. 41, No. 4, 2006, pp. 521–530.
doi:10.1007/s10697-006-0070-7

[13] Neiland, V., Sokolov, L., and Shvedchenko, V., "Temperature Factor Effect on the Structure of the Separated Flow Within a Supersonic Gas Stream," *Fluid Dynamics*, Vol. 43, No. 5, 2008, pp. 706–717.
doi:10.1134/S0015462808050049

[14] Korolev, G., Gajjar, J., and Ruban, A., "Once Again on the Supersonic Flow Separation near a Corner," *Journal of Fluid Mechanics*, Vol. 463, July 2002, pp. 173–199.
doi:10.1017/S0022112002008777

[15] Balakumar, P., Zhao, H., and Atkins, H., "Stability of Hypersonic Boundary Layers over a Compression Corner," *AIAA Journal*, Vol. 43, No. 4, 2005, pp. 760–767.
doi:10.2514/1.3479

[16] Fedorov, A., "Transition and Stability of High-Speed Boundary Layers," *Annual Review of Fluid Mechanics*, Vol. 43, No. 1, 2011, pp. 79–95.
doi:10.1146/annurev-fluid-122109-160750

[17] Verma, S., "Experimental Study of Flow Unsteadiness in a Mach 9 Compression Ramp Interaction Using a Laser Schlieren System,"

Downloaded by UNIVERSITY OF NOTRE DAME on July 2, 2018 | http://arc.aiaa.org | DOI: 10.2514/1.J056576

Measurement Science and Technology, Vol. 14, No. 7, 2003, pp. 989–997.
doi:10.1088/0957-0233/14/7/312

[18] Zhong, X., and Wang, X., "Direct Numerical Simulation on the Receptivity, Instability and Transition of Hypersonic Boundary Layers," *Annual Review of Fluid Mechanics*, Vol. 44, No. 1, 2012, pp. 527–561.
doi:10.1146/annurev-fluid-120710-101208

[19] Qin, F., and Xuesong, W., "Response and Receptivity of the Hypersonic Boundary Layer Past a Wedge to Free-Stream Acoustic, Vortical and Entropy Disturbances," *Journal of Fluid Mechanics*, Vol. 797, June 2016, pp. 874–915.
doi:10.1017/jfm.2016.287

[20] Sontag, J., and Gordeyev, S., "Non-Intrusive Velocity and Density Measurements in Subsonic Turbulent Boundary Layer," AIAA Paper 2015-3247, 2015.
doi:10.2514/6.2015-3247

[21] Raman, K. R., "Surface Pressure Fluctuations in Hypersonic Turbulent Boundary Layers," NASA CR-2386, Feb. 1974.

[22] Estorf, M., Radespiel, R., and Schneider, S., "Surface-Pressure Measurements of Second-Mode Instability in Quiet Hypersonic Flow," AIAA Paper 2008-1153, 2008.
doi:10.2514/6.2008-1153

[23] Casper, K., Beresh, S., Henfling, J., Spillers, R., and Pruett, B., "Hypersonic Wind-Tunnel Measurements of Boundary-Layer Transition on a Slender Cone," *AIAA Journal*, Vol. 54, No. 4, 2016, pp. 1250–1263.
doi:10.2514/1.J054033

[24] Smeets, G., and George, A., "Laser-Differential Interferometer Applications in Gas Dynamics," Institut Franco-Allemand De Recherches Saint Louis. Internal Rept. 28/73, St. Louis, France, 1996, translation by A. Goetz of the 1975 original (originally in French).

[25] Salyer, T., Collicott, S., and Schneider, S., "Feedback Stabilized Laser Differential Interferometry for Supersonic Blunt Body Receptivity Experiments," AIAA Paper 2000-416, 2000.
doi:10.2514/6.2000-416

[26] Parziale, N., Shepherd, J., and Hornung, H., "Differential Interferometric Measurement of Instability in a Hypervelocity Boundary Layer," *AIAA Journal*, Vol. 51, No. 3, 2013, pp. 750–754.
doi:10.2514/1.J052013

[27] Parziale, N., Shepherd, J., and Hornung, H., "Observations of Hypervelocity Boundary-Layer Instability," *Journal of Fluid Mechanics*, Vol. 781, Oct. 2015, pp. 87–112.
doi:10.1017/jfm.2015.489

[28] Baccarella, D., Liu, Q., Passaro, A., Lee, T., and Do, H., "Development and Testing of the ACT-1 Experimental Facility for Hypersonic Combustion Research," *Measurement Science and Technology*, Vol. 27, No. 4, 2016, pp. 1–12.
doi:10.1088/0957-0233/27/4/045902

[29] Smith, A., Gordeyev, S., Ahmed, H., Ahmed, M., Wittich, D., III, and Paul, M., "Shack-Hartmann Wavefront Measurements of Supersonic Turbulent Boundary Layers in the TGF," AIAA Paper 2014-2493, 2014.
doi:10.2514/6.2014-2493

[30] Leonov, S., Houpt, A., and Falempin, F., "Control of Hypersonic BL Transition by Electrical Discharge (Feasibility Study)," AIAA Paper 2015-3602, 2015.
doi:10.2514/6.2015-3602

[31] Raizer, Y. P., *Gas Discharge Physics*, Springer–Verlag, Berlin, 1991, p. 449.
doi:10.1007/978-3-642-61247-3

[32] Narayanaswamy, V., Raja, L., and Clemens, N., "Control of Unsteadiness of a Shock Wave/Turbulent Boundary Layer Interaction by Using a Pulsed-Plasma-Jet Actuator," *Physics of Fluids*, Vol. 24, No. 7, 2012, pp. 1–22.
doi:10.1063/1.4731292

[33] Tyson, R. K., *Principles of Adaptive Optics*, 3rd ed., CRC Press, Boca Raton, FL, 2011, pp. 117–183.
doi:10.1201/EBK1439808580

[34] Houpt, A., Gordeyev, S., Juliano, T., and Leonov, S., "Optical Measurement of Transient Plasma Impact on Corner Separation in $M = 4.5$ Airflow," AIAA Paper 2016-2160, 2016.
doi:10.2514/6.2016-2160

[35] Jumper, E. J., and Gordeyev, S., "Physics and Measurement of Aero-Optical Effects: Past and Present," *Annual Review of Fluid Mechanics*, Vol. 49, No. 1, 2017, pp. 419–441.
doi:10.1146/annurev-fluid-010816-060315

[36] Gonsalez, J. C., and Dolling, D. S., "Correlation of Interaction Sweepback Effects on the Dynamics of Shock-Induced Turbulent Separation," AIAA Paper 1993-0776, 1993.

[37] Sontag, J., and Gordeyev, S., "Studies of Density Fields in Non-Adiabatic Boundary Layers Using Wavefront Sensors," AIAA Paper 2017-3835, 2017.
doi:10.2514/6.2017-3835

[38] Liang, X., Li, X., Fu, D., and Ma, Y., "Effects of Wall Temperature on Boundary Layer Stability over a Blunt Cone at Mach 7.99," *Computers and Fluids*, Vol. 39, No. 2, 2010, pp. 359–371.
doi:10.1016/j.compfluid.2009.09.015

[39] Pröbsting, S., Scarano, F., Bernardini, M., and Pirozzoli, S., "On the Estimation of Wall Pressure Coherence Using Time-Resolved Tomographic PIV," *Experiments in Fluids*, Vol. 54, June 2013, pp. 1–15.
doi:10.1007/s00348-013-1567-6

[40] Farrell, B., and Ioannou, P., "Statistical State Dynamics-Based Analysis of the Physical Mechanisms Sustaining and Regulating Turbulence in Couette Flow," *Physical Review Fluids*, Vol. 2, No. 8, 2017, pp. 1–28.
doi:10.1103/PhysRevFluids.2.084608

[41] Biferale, L., Calzavarini, E., and Toschi, F., "Multi-Time Multi-Scale Correlation Functions in Hydrodynamic Turbulence," *Physics of Fluids*, Vol. 23, No. 8, 2011, pp. 1–6.
doi:10.1063/1.3623466

[42] Martin, M., Smits, A., Wu, M., and Ringuette, M., "The Turbulence Structure of Shockwave and Boundary Layer Interaction in a Compression Corner," AIAA Paper 2006-0497, 2006.
doi:10.2514/6.2006-497

[43] Dolling, D., and Or, C., "Unsteadiness of the Shock Wave Structure in Attached and Separated Compression Ramp Flows," *Experiments in Fluids*, Vol. 3, No. 1, 1985, pp. 24–32.
doi:10.1007/BF00285267

[44] Ganapathisubramani, B., Clemens, N., and Dolling, D., "Planar Imaging Measurements to Study the Effect of Spanwise Structure of Upstream Turbulent Boundary Layer on Shock Induced Separation," AIAA Paper 2006-0324, 2006.
doi:10.2514/6.2006-324

[45] Schneider, S., "Effects of High-Speed Tunnel Noise on Laminar-Turbulent Transition," *Journal of Spacecraft and Rockets*, Vol. 38, No. 3, 2001, pp. 323–333.
doi:10.2514/2.3705

[46] Mee, D., "Boundary-Layer Transition Measurements in Hypervelocity Flows in a Shock Tunnel," *AIAA Journal*, Vol. 40, No. 8, 2002, pp. 1542–1548.
doi:10.2514/2.1851

[47] Coles, D., "Measurements of Turbulent Friction on a Smooth Flat Plate in Supersonic Flow," *Journal of Aeronautical Science*, Vol. 21, No. 7, 1954, pp. 433–448.
doi:10.2514/8.3083

L. Ukeiley
Associate Editor